Numerical and Experimental Study of Damped Oscillating Manometers: I. Newtonian Fluids

JOHN C. BIERY

University of Wisconsin, Madison, Wisconsin

The time-dependent behavior of Newtonian oscillating manometers was studied experimentally and mathematically. The manometers were simulated by numerically integrating the axial component of the equation of motion in cylindrical coordinates. Modifications in the driving-force term were made to include end effects of surface tension and flow reversal. The integrations showed that the velocity profiles in the manometer were not parabolic and contained many maxima and minima, particularly when the fluid had a low viscosity. Good agreement was obtained between experimental and simulation frequencies and damping factors.

The oscillating manometer provides a simple system with which to test the time-dependent rheological properties of non-Newtonian fluids. However, before the manometer can be used in non-Newtonian tests, the time-dependent behavior of Newtonian fluids in the manometer must be well known. A study of previous mathematical developments (*1, 2, 3, 4, 5*) describing the oscillating manometer revealed that overall force or mechanical energy balances had been employed with the assumption that the velocity profile within the manometer had a constant shape, usually parabolic, at all times with the amplitude a function of time. With this assumption, the force balance and the mechanical energy balance led to two different differential equations and also to results which did not agree with experimental data for manometers containing low-viscosity fluids. As a result, the efforts reported here were initiated to develop a satisfactory simulation of the Newtonian oscillating manometer.

To simulate the time-dependent behavior of the oscillating manometer, the axial component of the equation of motion in cylindrical coordinates was numerically integrated on a digital computer. The driving force in the equation was modified by end-effect corrections to take into account surface tension and flow reversal at the ends of the moving columns. The integrations were compared with thirteen experimental runs with three diameter tubes and five Newtonian fluids with varying viscosities. The agreement between experimental and simulation damping factors and cycle times was very good. Also, the numerical calculations showed that the velocity profiles in the manometer are extremely distorted and deviate greatly from a parabolic configuration. The results indicated that non-Newtonian rheological models could be tested by using similar integration procedures modified by the appropriate end-effect corrections.

EXPERIMENTAL EQUIPMENT, PROCEDURE AND RESULTS

Equipment Description

The manometers used in the experimental study were formed from soft glass tubing and had the dimensions indicated in Figure 1 and in Table 1.

John C. Biery is with the Los Alamos Scientific Laboratory, Los Alamos, New Mexico.

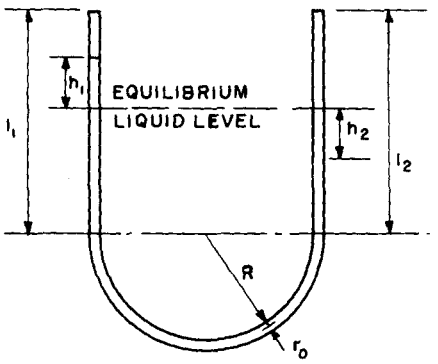

Fig. 1. Manometer with characteristic dimensions.

The radius of the bend was made as large as possible to minimize the distortion of the laminar streamlines around the bend. With small radius bends, a significant flow perpendicular to the longitudinal axis would exist. In making the bends, the tubing was slightly necked down in the curved region. The degree of necking is indicated by the radii of the tube in the straight and curved sections. The radii of these sections were determined by weighing the quantity of water required to fill the respective sections.

Auxiliary items of equipment were an electric stop watch for measuring cycle times, a mercury thermometer for recording room and fluid temperatures, and a rubber tube with bleed valve and rubber stopper for applying air pressure to one leg of the manometer. The stop watch could be read to within ± 0.01 sec. while the thermometer was accurate to ± 0.1°C. The amplitudes of the moving fluid were measured

TABLE 1. MANOMETER TUBE DIMENSIONS

Tube no.	Straight section length, cm. l_1	Straight section length, cm. l_2	Bend radius cm.	Tube inside radius, cm. Straight section	Tube inside radius, cm. Curved section	Total length along center line, cm.
1	32.45	28.60	19.69	1.267	1.251	122.89
2	30.28	30.28	20.04	1.078	1.052	123.52
3	31.90	30.25	19.53	0.4602	0.4545	123.51

Table 2. Equivalent Dimensionless Time Units

Manometer no.	Radius, cm.	No. of units equivalent to 0.01 sec.
1	1.25	0.34
2	1.05	0.37
3	0.45	0.57

with a scale which could be read to within ± 0.02 cm.

Viscosities for the Newtonian fluids utilized in the experiments were checked by running samples on a cone-and-plate viscometer (*6, 7*). The data obtained on the viscometer checked within ± 2% of the values presented in standard tables (*8*) and as a result, the tabular values for all solutions were utilized. The densities of the fluids required to check the viscosities from the tables were determined by weighing samples in a 25 ml. pycnometer at 25°C.

Experimental Procedure

Startup. The legs of the manometer were brought into imbalance by applying air pressure to the right-hand leg. When the legs were stationary at the desired height position, the air supply was quickly removed, and the fluid was allowed to oscillate freely. The air pressure was supplied to the glass tube through a hose connected to a rubber stopper. The air pressure was removed by removing the stopper. Thus, no airflow restriction existed in the end of the tube. However, on the first one-half cycle, some added damping existed while the higher pressure air flowed out of the manometer tube.

Cycle-Frequency Measurements. The oscillation cycle times* were determined by measuring to the nearest 0.01 sec. the time required for the fluid to oscillate from initial start-up to the desired maximum or minimum in amplitude of the particular cycle of interest. The timer was started and stopped with a manual switch. The instant for stopping the timer was determined by visually observing the maximum in amplitude. This method of measuring the cycle times produced random errors owing to human reflexes and judgement; therefore, for each cycle time many observations were made, and the average of the times was taken as an estimate of the actual cycle time. The standard deviations, range of time measurements, and confidence interval for the measurements are given in Table 6 in the Appendix.†

In Table 6, the cycle-time observations were assumed to come from a normally distributed population. The estimated standard deviations were obtained from the range of data and the number of observations, and the confidence interval of the mean was obtained by applying the student t test (*9*).

The measurement of one cycle time by subtracting two consecutive cycle-time measurements had 90% confidence intervals ranging from ± 0.04 to ± 0.06 sec. See Table 2 for equivalence between real time and dimensionless time units for the three manometers. For the no. 1 manometer, these times correspond to ± 1.4 to 2.0 dimensionless units. However, if the unit cycle times after the first cycle are assumed to be constant, the average cycle time obtained by subtracting the time of the first complete cycle from the nth cycle time and dividing by n — 1 had confidence intervals ranging from ± 0.007 sec. to ± 0.025 sec. For the low-viscosity fluids which oscillated for many cycles, the average cycle time was measured quite accurately. However, for the fluids that oscillated from one-half to one cycle, the confidence interval was quite large, ± 0.035 sec., when compared to the total time of 1.0 to 1.5 sec. being measured.

The amplitude of each oscillation was measured by adjusting rubber bands on the outside of the tube to correspond to the maximum and minimum position of the liquid meniscus in each leg for each cycle. The band was positioned correctly when the meniscus just touched the lower edge of the band on the upstroke or just appeared below the band on the downstroke. A light background was used to illuminate brightly the meniscus and indicate the point of contact. No statistical replications of the height measurements were made; however, the errors involved in the measurements were believed to be less than ± 1% for heights greater than 5 cm. and ± 0.05 cm. for heights below 5 cm.

The errors in the calculated damping factors* depend upon the height range involved. For instance, an amplitude decrement from 10 to 5 cm. in half of a cycle could result in measured damping factors from 0.221 to 0.209 from the uncertainties listed above. This range gives a bond of ± 3% in which the actual damping factor could lie. Similarly, a decrement from 10 to 1 cm. would have errors of ± 1.5% about the

* One full-cycle period is the time required for the legs to return to a maximum position similar to the initial position. A half-cycle period is the time required to attain a minimum position with the legs reversed relative to the initial position.

† The Appendix to this paper has been deposited as document 7638 with the American Documentation Institute, Photoduplication Service, Library of Congress, Washington 25, D. C., and may be obtained for $2.50 for photoprints or $1.75 for 35-mm. microfilm.

* The amplitude decrement data were analyzed by applying the standard second-order damped harmonic differential equation solution to each half cycle (*10*). Thus, if this equation did not apply over the whole time range, the damping factor would vary from cycle to cycle. The differential equation is as follows:

$$\frac{d^2h^*}{dt^{*2}} + 2\omega_n \zeta \frac{dh^*}{dt^*} + \omega_n^2 h^* = 0 \qquad (1)$$

where ζ is the damping factor and ω_n is the natural frequency of the system. This equation has the following underdamped solution:

$$h^* = \frac{h_0^*}{\omega} e^{-\zeta t^* \omega_n} \left[\sin\left(\omega \omega_n t^* + \tan^{-1} \frac{\omega}{\zeta} \right) \right]; \quad \omega = \sqrt{1 - \zeta^2} \qquad (2)$$

When the amplitudes of the harmonic motion are known, the damping factor can be calculated from

$$\frac{\zeta^2}{1 - \zeta^2} = \left[\frac{1}{n\pi} \ln \left(\left| \frac{h^*_a}{h^*_b} \right| \right) \right]^2 \qquad (3)$$

where n is the number of half cycles between height measurements, h^*_a and h^*_b.

Table 3. Experimental Conditions for Manometer Runs

Run no.	Fluid type: Aqueous solution of	Weight, %	Temp., °C.	Fluid density	Fluid viscosity, centipoise	Fluid length, cm.	Tube radius,* cm.
20	Water	100.00	23.0	0.9975	0.9358	91.27	1.256
21	Glycerine	48.49	23.5	1.120	4.91	90.82	1.256
22	Glycerine	72.46	23.4	1.186	23.8	76.37	1.254
24	Sucrose	65.18	24.0	1.315	116.0	89.35	1.256
31	Water	100.00	24.0	0.9973	0.9143	89.52	1.058
32	Glycerine	48.49	24.0	1.119	4.75	91.05	1.059
33	Glycerine	72.46	24.8	1.185	21.6	90.82	1.059
34	Glycerine	82.04	24.2	1.211	58.0	92.22	1.059
35	Sucrose	65.18	24.2	1.315	114	90.62	1.059
41	Water	100.00	24.1	0.9973	0.9101	88.16	0.4562
42	Glycerine	48.49	24.2	1.119	4.75	91.36	0.4564
43	Glycerine	72.46	24.0	1.185	22.3	91.40	0.4564
44	Glycerine	82.04	24.0	1.212	58.5	90.91	0.4563

* The tube radius is an average of the curved and straight section radii weighted by the length of fluid in each section.

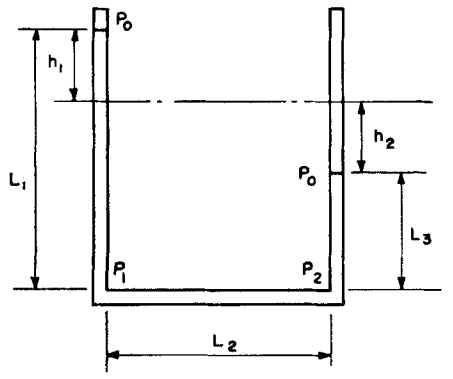

Fig. 2. Rectangular manometer for illustrative example.

mean damping factor of 0.590. The errors below 1 cm. are much greater. A change from 1 to 0.5 cm has an error of ± 21% about the 0.215 damping factor. Also, from 1 cm. to 0.1 cm., the error band is ± 16% about an average factor of 0.600.

Experimental Results

In Table 3 the experimental conditions that existed during each manometer run are tabulated. In Table 7 in the Appendix are found the experimental amplitude and cycle-time measurements that were determined in each run.

MATHEMATICAL SIMULATION

Without the Inclusion of Secondary Effects

The velocity profile and, as a result, the average velocity of the fluid in the manometer can be determined by numerically integrating the axial component of the equation of motion in cylindrical coordinates which have the following form with the assumptions that $v_r = 0$, $v_\theta = 0$, and $v_z = v_z(r, t)$ *.

$$\rho \frac{\partial v_z}{\partial t} = \left(-\frac{\partial P}{\partial z} + \rho g_z \right) + \mu \left[\frac{1}{r} \frac{\partial}{\partial r} \left(r \frac{\partial v_z}{\partial r} \right) \right] \quad (4)$$

The dimension z is taken along the center line of the tube and is positive when directed upward along the left-hand tube (Figure 1). Also, the surface levels of the liquid in the two legs are indicated by h_1 for the left leg and h_2 for the right leg. The quantities h_1 and h_2 are positive in the positions shown in Figure 1.

The forcing function $\left(-\frac{\partial P}{\partial z} + \rho g_z \right)$ is independent of position and for the manometer equals $\rho g(h_1 + h_2)/L_{\text{total}}$. A simple example with a right-angle manometer shown in Figure 2 helps to indicate the validity of the above statement:

$$\left(-\frac{\partial P}{\partial z} + \rho g_z \right) = -\frac{\partial \mathcal{P}}{\partial z} =$$

$$\frac{P_0 - P_1}{L_1} + \rho g = \frac{P_1 - P_2}{L_2} = \frac{P_2 - P_0}{L_3} - \rho g \quad (5)$$

$$-P_1 + P_2 = \frac{\partial \mathcal{P}}{\partial z} L_2 \quad (6)$$

$$P_0 - P_1 = -\rho g L_1 - \frac{\partial \mathcal{P}}{\partial z} L_1 \quad (7)$$

$$-P_0 + P_2 = \rho g L_3 - \frac{\partial \mathcal{P}}{\partial z} L_3 \quad (8)$$

$$\rho g(L_3 - L_1) - \frac{\partial \mathcal{P}}{\partial z}(L_1 + L_3) = \frac{\partial \mathcal{P}}{\partial z} L_2 \quad (9)$$

$$-\frac{\partial \mathcal{P}}{\partial z} = \frac{(L_1 - L_3)\rho g}{L_1 + L_2 + L_3} = \frac{(h_1 + h_2)\rho g}{L_{\text{total}}} \quad (10)$$

With dimensionless variables and $h_1 = h_2 = h$, the equation of motion takes the following form:

$$\frac{\partial v_z^*}{\partial t^*} = -\frac{4}{3}\frac{h^*}{L^*} + \left(\frac{1}{6\Omega_1} \right) \frac{1}{r^*} \frac{\partial}{\partial r^*} \left(r^* \frac{\partial v_z^*}{\partial r^*} \right) \quad (11)$$

The average velocity is obtained by integrating the velocity profile over the area of the tube:

$$\frac{dh^*}{dt^*} = \langle v_z^* \rangle = 2 \int_0^1 v_z^* r^* dr^* \quad (12)$$

The dimensionless groups are listed below:

$$t^* = t \left(\frac{3}{2} g/r_o \right)^{1/2}$$

$$h^* = h/r_o$$

$$v^* = v \left(\frac{3}{2} r_o g \right)^{-1/2}$$

$$L^* = L/r_o$$

$$r^* = r/r_o$$

$$\Omega_1 = \left(\frac{1}{24} g r_o^3 \right)^{1/2} \left(\frac{\rho}{\mu} \right)$$

The solution of the above equations in closed form is not readily obtained; therefore, the equations were integrated numerically on a digital computer. With k, the radial grid index, and m, the time grid index, the equations assumed the following form when the derivatives were replaced with first-order difference approximations:

$$v^*_{k,m+1} = v^*_{k,m} - \left(\frac{4}{3} \right) \frac{\Delta t^*}{L^*} h^*_m + \left(\frac{\Delta t^*}{6\Omega_1 (\Delta r^*)^2} \right) \left[\left(1 + \frac{1}{2k} \right) v^*_{k+1,m} - 2v^*_{k,m} + \left(1 - \frac{1}{2k} \right) v^*_{k-1,m} \right] \quad (13)$$

At the center line, Equation (14) was used; Equation (13) is indeterminate with k equal to zero for the center position:

$$v^*_{o,m+1} = v^*_{o,m} - \left(\frac{4}{3} \frac{\Delta t^*}{L^*} \right) h^*_m + \left(\frac{4\Delta t^*}{6\Omega_1 (\Delta r^*)^2} \right) [v^*_{1,m} - v^*_{o,m}] \quad (14)$$

---

* These assumptions ignore the effects of the curved section in the manometer. The curvature forces some fluid to flow radially. With a large radius curve, this effect was minimized. When the ratio r_o/R is smaller the effect is smaller.

The increase in friction factor owing to the curvature in steady flow around a curved pipe when compared to flow through a straight pipe has been correlated as a function of

$$\left(\frac{r_o}{R} \right)^{1/2} \left(\frac{2 r_o \langle v \rangle \rho}{\mu} \right)$$ (See reference 13).

The experimental data from all of the runs were analyzed with the above correlation to determine whether or not curvature effects could be significant. The maximum average velocity in each cycle was used in the analysis. The correlation indicated that curvature effects did not exist in cycles 3 and 4 of run 22, all of run 24, cycles 2, 3, and 4 of run 33, all of runs 34, 35, 43, and 44, and the last cycle of runs 41 and 42. Curvature effects were indicated to be significant for runs 20, 31, and 41. For these last runs the curved-pipe friction factor was at least twice the straight-pipe friction factor at the maximum velocities used. As indicated in the conclusions section, the curvature effect appeared to be negligible for all runs other than 20, 31, and 41.

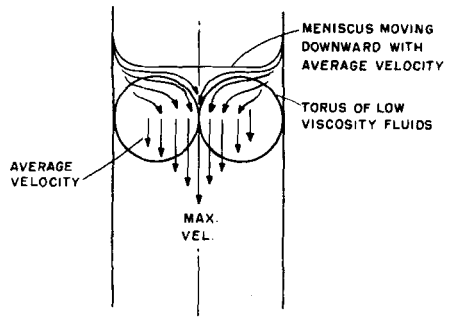

Fig. 3. Flow reversal at end of manometer fluid.

The average velocity was obtained by numerically integrating the velocity profile over the tube area by repeatedly using Simpson's integration rule (*11*)

$$<v^*>_m = \frac{2}{3}(\Delta r^*)^2 [4v^*_{1,m}(1) + 2v^*_{2,m}(2) + 4v^*_{3,m}(3) + \ldots + 4v^*_{K-1,m}(K-1)] \quad (15)$$

where K is the number of radial subdivisions.

The new interface position of the manometer fluid is found by integrating the average velocity over the time increment with the modified Euler formula.

$$h^*_{m+1} = h^*_m + 1/2\,(<v^*>_{m+1} + <v^*>_m)\Delta t^* \quad (16)$$

With Equations (13), (14), (15), and (16), the approximate velocity profile can be obtained as a function of time. First the velocity profile is determined, then the average velocity is found, and finally the change of manometer position is calculated. With the new h^*, the operation can then be repeated for the next time increment.

The velocity profiles and the overall time behavior obtained by the numerical integration method are only approximate because of the truncation errors involved. However, when the Δr^* and Δt^* grid were sufficiently refined, the h^* values, velocity profiles, and damping factors converged quite rapidly. The degree of refinement depended greatly on the viscosity of the fluid in the manometer. For a viscous fluid, 0.5 to 1.0 poise, the equations with $\Delta t^* = 0.05$ and $\Delta r^* = 0.1$ closely approximated the final answer. However, for a 0.01 poise fluid a $\Delta t^* = 0.0125$ and $\Delta r^* = 0.0125$ grid produced results which still fell somewhat short of the final extrapolated values. The rate of convergence was determined to be rapid, however, in that the size of $\Delta\zeta$, the change in damping factor for a halving of the grid dimensions, was approximately one-third the size of the previous $\Delta\zeta$ for the previous grid change. Thus, the final damping factors could be estimated by running integrations at two grid sizes and then proceeding to estimate additional change with the one-third factor rule.

Inclusion of End Effects

The equations as developed above approximately describe the Newtonian oscillating manometer. To obtain a more accurate simulation, various end effects must be included in the equations. Three major end effects should be considered. These are flow reversal, surface tension, and falling-film effects.

Flow Reversal. The velocity profiles at the ends of the oscillating fluid are extremely distorted and are quite different from the profiles that exist in the main body of fluid. In Figure 3, the flow pattern at the end of the fluid moving downward is sketched. Fluid nearly stationary along the wall must suddenly accelerate and flow along the meniscus surface into the high-veocity center portion of the stream. All fluid flowing slower than the velocity of the meniscus, which is the average velocity of the fluid, must flow toward the center of the tube into a region of velocity greater than the average velocity. For viscous fluids, the streamlines are quite smooth, but for low-viscosity fluids like water, the fluid tends to rotate in a large toroidal shaped mass.

This end effect was empirically included in the differential equation by subtracting a pressure term equal to the retarding effect of the flow reversal. The retarding force was postulated to have the following form:

$$F_T = K_T S r_o <v_z> \mu \quad (17)$$

The subscript, T, stands for torus.
K_T is an arbitrary constatnt, and Sr_o is proportional to the volume of the rotating torus. The retarding force was assumed to be proportional to the fluid viscosity and some characteristic velocity since the retarding viscous force in steady state pipe flow is proportional to these two terms. To include this term in the differential equations, F_T was divided by the cross-section area, S and L to put it in the $\Delta P/L$ form. In dimensionless form, this term becomes

$$\frac{P^*_T}{L^*} = \frac{4}{3}\frac{<v^*>}{L^*}\Omega_2;\ \Omega_2 = \frac{\sqrt{3/8}\,K_T r_o^{1/2}\mu}{\rho g^{1/2}} \quad (18)$$

This term, P^*_T/L^*, is included in Equations (13) and (14) by subtracting it from the right side of each equation. K_T is evaluated from the experimental data as described below.

Surface Tension. If the contact angles between the liquid and the manometer tube are not equal at the receding and advancing ends of the manometer liquid, then a retarding force owing to surface tension must be included. With a fluid tube system where the contact angles of both surfaces are very close to 0°, the retarding effect is negligible. However, if a nonwetting tube is used, the contact angle changes drastically between an advancing and receding motion. To account for this effect, a surface tension force term must be subtracted from the right side of Equations (13) and (14). The net force exerted by the surface on the solid is given below:

$$F_{ST} = 2\pi r_o K_{ST}(\cos\phi_R - \cos\phi_A) \quad (19)$$

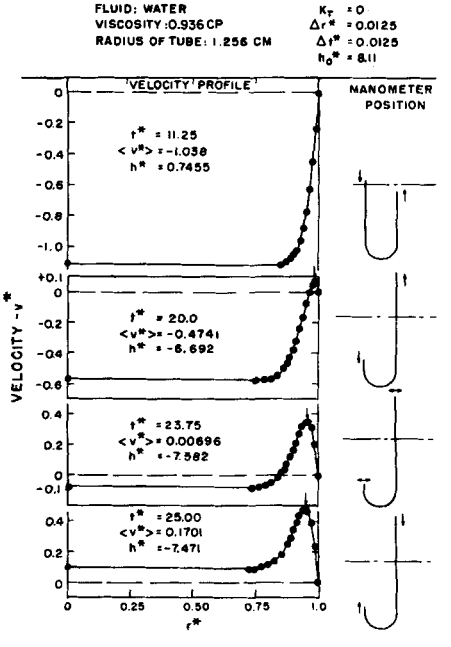

Fig. 4. Velocity profiles of run 20.

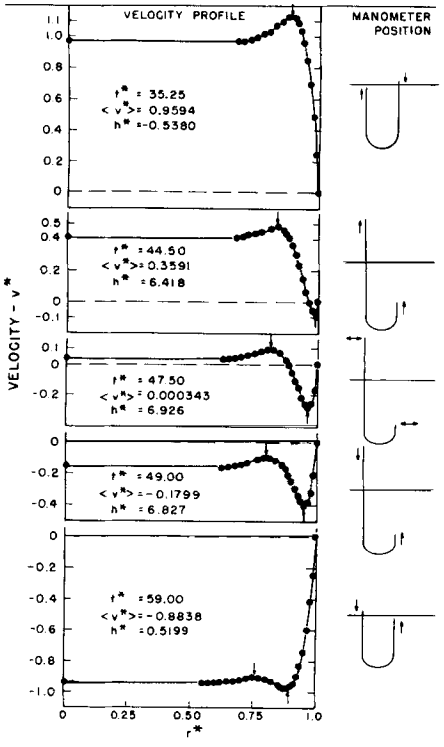

Fig. 5. Velocity profiles of run 20.

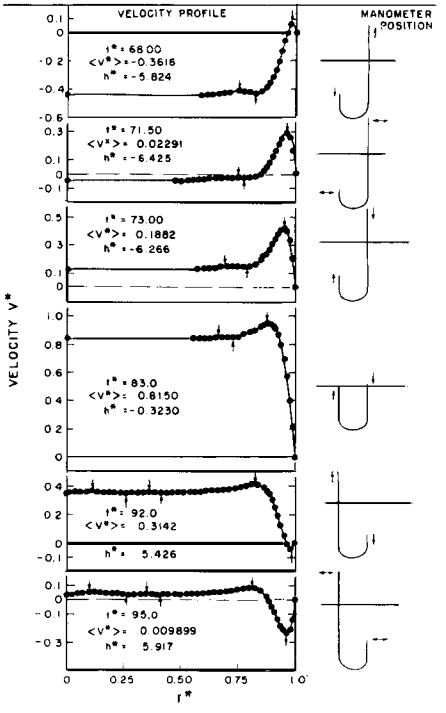

Fig. 6. Velocity profiles of run 20.

When reduced to dimensionless form, the term to be subtracted is

$$\frac{P_{ST}^*}{L^*} = \frac{4}{3}\Omega_3 M/L^* \qquad (20)$$

where M is defined by $\langle v^* \rangle = M|\langle v^* \rangle|$ and $\Omega_3 = \dfrac{K_{ST}(\cos\phi_R - \cos\phi_A)}{r_0^2 \rho g}$

Falling Film. When the liquid wets the walls of the tube, a film of liquid is left on the tube by the receding liquid and is partly picked up by the rising liquid on the return stroke. This effect reduces the mass of the system temporarily and changes the instantaneous equilibrium position of the manometer legs. For the analysis presented here, this effect is ignored. When the experimental data are analyzed, the average leg height, $(h_1 + h_2)/2$, is used at all times as the height above the equilibrium position.

Additional mathematical analysis indicated that the influence of the falling film on the damping factor, except for very viscous fluids with a ζ near 1.0, is quite small. However, the cycle times are reduced from 0 to 10% by the falling film. The analysis including the falling film will be presented elsewhere.

Simulation Results

The simulation results are presented in Table 4 and in Table 9 in the Appendix. The values of ζ and cycle times

Table 4. Summary of Simulation and Experimental Data for Newtonian Oscillating Manometer Runs

		Average cycle time—(dimensionless units)				Average damping factor			
			Simulation				Simulation		
Run no.	K_T, cm.$^{-2}$	Experimental	Without K_T	With K_T	% error* with K_T	Experimental	Without K_T	With K_T	% error*† with K_T
20	288	48.3	47.7	47.7	−1.1	0.0303	0.0262	0.0303	0
21	70.6	49.6	49.0	49.0	−1.4	0.0659	0.0613	0.0659	0
22	56.1	48.9	47.8	47.8	−2.4	0.157	0.140	0.157	0
24	41.6	30.4	29.8	31.0	+2.0	0.477	0.430	0.477	0
			(Last half of first cycle)						
31	192.8	52.2	51.5	51.5	−1.4	0.0338	0.0305	0.0338	0
32	74.2	54.7	54.0	54.0	−1.3	0.0765	0.0729	0.0765	0
33	60.0	59.7	58.0	58.5	−2.0	0.183	0.171	0.183	0
34	59.0	66.6	63.3	64.5	−3.2	0.373	0.343	0.373	0
35	72.2	75.1	72.8	77.8	+3.6	0.648	0.582	0.648	0
41	200	81.3	81.3	81.3	0	0.0787	0.0793	0.0804	+2.0
42	247	86.9	89.5	89.8	+3.3	0.202	0.197	0.202	0
43	210	66.4	61.0	61.5	−7.3	0.702	0.677	0.702	0
			(First half of first cycle)						
Avg. % error:					−0.68%				+0.17%

* % error = (simulated-experimental)(100)/experimental.

† K_T was chosen to adjust the damping factor % error to zero. Run 41 was arbitrarily simulated with K_T equal to 200 to show the relatively small size of the end effect and the relative uncertainty of the end effect in the small diameter tube.

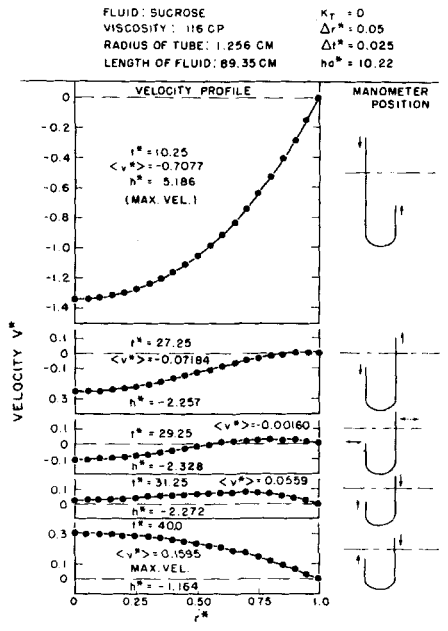

Fig. 7. Velocity profiles of run 24.

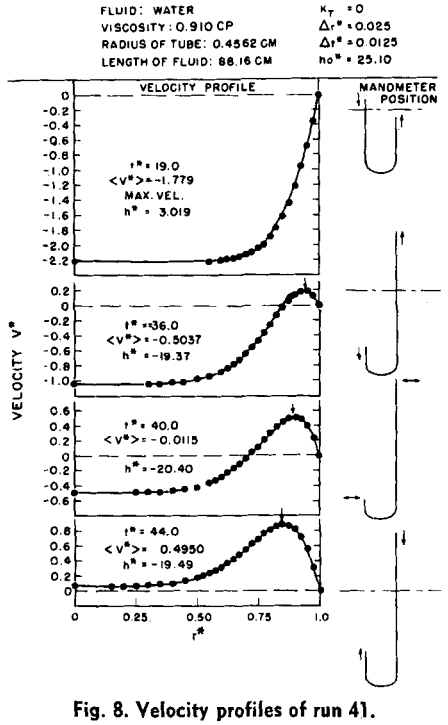

Fig. 8. Velocity profiles of run 41.

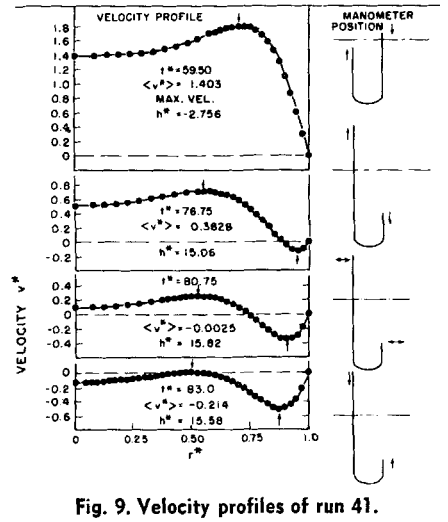

Fig. 9. Velocity profiles of run 41.

given are those estimated at convergence by using the 1/3 factor procedure previously described. Also, the damping factors and cycle times are presented for the cases of $K_T = O$ and K_T equal to the value which best simulated the experimental conditions after the first few cycles. In Table 8 in the Appendix, the simulation data is given as obtained from the computer for the various grid sizes.

VELOCITY PROFILES

One of the more interesting results of this investigation was the generation of the velocity profiles existing in the manometer by the numerical integration of the equation of motion. When the dynamics of an oscillating manometer are described, the velocity profiles often are assumed to be parabolic. As can be seen in Figures 4 through 9, the velocity profiles differ markedly from the parabolic profile. The parabolic profiles are approached only in fluids with high viscosity and/or in manometers with small diameters.

That the velocity profiles for an oscillating fluid bounded by solid surfaces are not parabolic is not wholly an unexpected result. A problem involving sinusoidal motion of a fluid next to a solid plane was presented by Lamb (*12*), and a diagram of the position profiles to be expected for this problem is presented on page 622 of the reference *12*. The oscillating manometer profiles are more complicated than the ones for simple harmonic motion next to a plane because of the varying amplitude of vibration which produces different velocity configurations for succeeding cycles.

In the velocity profiles shown in Figures 4 through 9, the ones for the 116-centipoise viscosity solution of sucrose shown in Figure 7 approach the parabolic profile for most of the stroke length; but even in this fluid, the profiles deviate at the ends of the stroke. The other profiles are shown for water in the 1.256- and 0.456-cm. radius tubes. As can be seen for this low-viscosity fluid, the effect of the wall does not travel very rapidly into the body of the fluid. Most of the fluid tends to maintain a flat profile in the first few strokes. On each stroke, a new distortion wave is generated, and this wave travels into the body of the fluid. Run 20 profiles show that the wave crest is maintained through a number of succeeding strokes. Each stroke generates one crest, and, as a result, the first half of the first cycle shows one maximum; the last half of the first cycle shows one maximum and one minimum. An interesting effect is shown in Figure 6 in that more maxima and minima are present that should appear. This phenomenon results from the waves that reach the center of the tube and are either reflected or transmitted on into the other half of the tube. The generation of the new wave at the edges of the tube starts before the manometer fluid reaches the end of its stroke. While the bulk of the fluid is still flowing in a downward direction, for instance, the fluid at the edge of the tube has reversed direction and is flowing upward. This phenomenon has the unusual property of producing a force at the wall which tends to help the fluid to flow in its macroscopic direction of flow near the end of the stroke. The maxima and minima are marked with small arrows in Figures 4 through 9.

With the velocity profile varying in shape for each stroke, the damping factor tends to oscillate about a mean value that is approached after three or four oscillations. As can be seen in the simulation data of Table 8, the damping factor on the first half cycle is low while the factor on the second half cycle is high. The succeeding factors continue to oscillate about the steady state value with diminishing deviations. This effect is very pronounced for the low-viscosity solutions in large diameter

manometers and is quite insignificant in high-viscosity solutions in small diameter tubes.

RESULTS AND CONCLUSIONS

In Table 4 the steady state experimental and simulated damping factors and cycle times are compared for each run. As can be seen, the agreement is in general very satisfactory. The low-viscosity solutions gave the best results because more cycles could be measured, the amplitude decrement was quite low, and the falling-film effect was minimal. In the high-viscosity solutions, the measurements for the small amplitude strokes had the greatest relative error, and therefore, agreement betwen the simulated and experimental data should be less satisfactory. As indicated in Table 4, the steady state damping factors were adjusted with the appropriate K_T values to obtain, in general, exact agreement with the experimental values. However, the cycle times shown also agreed very well with the experimental times. For the twelve runs reported, the simulated times were on an average 0.7% smaller than the experimental times. The standard deviation of the time errors was 2.5%, and a student t test indicated that there was no significant difference between the 0.7% error and 0% error of perfect simulation.

An analysis of the simulation data for each cycle of each run is shown in Table 9 in the Appendix. The Newtonian manometer data were analyzed in this manner to indicate the error ranges, standard deviations, and levels of significance for comparison with similar non-Newtonian data obtained on the same manometers. The non-Newtonian data must be analyzed on a per cycle basis since the damping factors and cycle times for non-Newtonian fluids will vary as the amplitude of oscillation decreases. The per cycle data for the Newtonian fluids indicate that the first cycle was damped somewhat excessively by the efflux of the air required to unbalance the legs for initial start-up. The effect, however, was noticeable only with fluids and tubes which had damping factors below 0.2. The increase in damping in the first cycle owing to the air efflux increased with decreasing tube radius. The average percent error in the first cycle for the low-viscosity fluids was − 9% for the 1.256-cm. radius tube, − 13% for the 1.06-cm. radius tube, and − 20% for the 0.456-cm. radius tube. The values for the first cycle from the low-viscosity fluids were not included in the overall averages reported below.

The statistical analysis of the per cycle data is summarized below:

Damping factors

Error range*	−11 + 10%
Average error, $\bar{x}$	+0.87%
Number in average	30
Sum of squares	414
Sum mean square, s^2	414/29 = 14.3
Sample standard deviation, s	3.8%
Sample standard deviation of mean, $s_{\bar{x}}$	0.69%

Student t hypothesis test hypothesis: $\bar{x} = 0$

$$t = \frac{\bar{x} - 0}{s_{\bar{x}}} = 1.26 \text{ (statistically significant at 20\% level)}$$

* % error = (simulated-experimental)(100)/simulated).

Cycle times

Error range	−13 + 4%
Average error, $\bar{x}$	−2.3%
Number in average	24
Sum of squares	312
Sum mean square, s^2	13.5
Sample standard deviation	3.7%
Sample standard deviation of mean, $s_{\bar{x}}$	0.75%

Student t hypothesis test hypothesis: $x = 0$

$$t = \frac{\bar{x} - 0}{s_{\bar{x}}} = -3.07 \text{ (significant at 99\% level)}$$

An interesting development from the above analysis is that the − 2.3% difference between simulated and experimental cycle times was significantly different statistically from the desired zero percent error. The data in Table 4 shows that the cycle time errors for the steady state cycles were not significantly different from zero, while the analysis including the initial cycles in Table 9 shows a statistically significant difference from zero. However, in both cases, the percentage error is small, and it shows that the simulation is quite satisfactory. The increased error of the initial cycles could be owing to some of the assumptions of the simulation such as ignoring tube-curvature effects, falling-film effects, and air-flow effects. The per cycle analysis also shows the simulation damping factors to be 0.87% higher than the experimental damping factors. This value is not statistically different from zero percent error.

The inclusion of the reversal end effect was necessary to obtain good simulation agreement. The value of K_T was varied for each run to produce the best simulation*.

TABLE 5. REVERSAL END EFFECT, K_T VALUES

Run no.	Viscosity, centipoise	Tube radius, cm.	K_T, cm.$^{-2}$	Avg. K, cm.$^{-2}$
20	0.9358	1.256	288	
21	4.91	1.256	70.6	
22	23.8	1.254	56.1	56.1
24	116	1.256	41.6	
31	0.9143	1.058	192.8	
32	4.75	1.059	74.2	
33	21.6	1.059	60.0	66.3
34	58.0	1.059	59.0	
35	114	1.059	72.2	
41	0.9101	0.4562	200	
42	4.75	0.4562	247	228.6
43	22.3	0.4562	210.5	

In Table 5 is presented a summary of the K_T values required by each run. The end effect adjusted the damping factors from 10 to 15% in the 1.256-cm. tube, approximately 10% in the 1.059-cm. tube, and about 5% in the 0.456-cm. tube. The K_T values appeared to be somewhat constant for a given tube size except for the low-viscosity water runs.

When the value of K_T was adjusted to obtain agreement between experimental and simulation damping factors, the end-effect correction was forced to include all anomalies not included in the simulation equations. Two such effects were turbulence and nonlinear flow patterns owing to tube curvature. A calculation of Reynolds numbers with the maximum average velocity of each stroke showed that turbulence could exist during these maximum velocity periods in runs 20, 31, and 41. Also, as previously indicated, curvature effects were probably significant in these same runs. The use of the curvature correlation (*13*) indicated that some increase in damping factor might also be expected in the first few cycles of runs 21, 22, 33, and 42. However, since the increased damping owing to curvature decreases with decreased velocity, the

* Only one simulation for each run with K_T set at same reasonable value need be run. The value of $\Delta\zeta/K_T$ was constant for each run, and once the ratio was determined, the correct value of K_T could be directly calculated.

experimental damping factors should decrease in the low-amplitude cycles where the curvature effects were shown to be negligible from the above correlation.. That this decrease in damping factor was not observed would indicate that curvature effects were negligible during the duration of each of the questionable runs. Also, the K_T values should be significantly lower for the high-viscosity runs where the curvature effects did not exist. As can be seen in Table 5, the K_T values remained almost constant for all runs of a given size tube except for runs 20, 31, and possibly 21. This agreement in K_T values would also indicate that curvature effects were minimal in all of the other runs.

The turbulent action in runs 20 and 31 was observed visually in the reversal flow at the ends of the tube. In these runs, the toroidal action at the end of the tube was observed to produce a torus which did not reverse smoothly at the end of the stroke, but which appeared to explode in the reversing acton. This effect was observed by placing particles in the fluid at the end of the tube and noting their movement with the fluid. For the higher viscosity fluids, the streamlines at the end of the fluid column appeared to be smooth. This turbulent action in water produced higher K_T values as can be seen in runs 20 and 31.

The average K_T values were not constant for different diameter tubes. The smaller the tube, the larger the value of K_T. This variation suggested that the original hypothesized form for the force at the end of the tubes should have had a form where $K_{end} = r_o K_T$. With this change, the K_{end} values obtained are as follows:

Tube radius (cm.)	K_{end} (cm.$^{-2}$)
1.256	70.5
1.059	70.3
0.4563	104.2

The end force would then have the form: $F_T = K_{end} S \langle v_z \rangle \mu$.

The surface-tension term was not tested extensively since in most of the manometers tested, the fluid wetted the tube walls and the contact angles for both receding and advancing columns were 0 deg. The meniscus for the receding stream was greatly deepened and for the advancing column was greatly flattened. However, the contact angle for both columns still appeared to remain at 0 deg.

One experiment not reported in the above tables was run in which water was oscillated in a Tygon manometer tube. The water did not wet the plastic, and the contact angle for the advancing column was about 105 deg. while for the receding column was about 75 deg. This surface-tension effect caused the damping factor to increase as the amplitude became smaller, and at a limiting position, the oscillation stopped even though the legs were slightly out of balance. In simulation of this run, the surface-tension effect end term produced this type of action.

The above reported results suggest that the oscillating manometer can be used as a rheological model testing device. To be able to discriminate between rheological effects and simulation effects, the equation of motion should be numerically integrated. Also, to eliminate errors in damping factors of from 5 to 15%, the flow-reversal end effect should be included in the simulation equations. With this modification, the comparison of experimental and simulation data should indicate the validity of using the particular rheological equation under the unsteady state conditions existing in the oscillating manometer. The study of non-Newtonian flow in oscillating manometers will be discussed in a subsequent paper.

ACKNOWLEDGMENT

The author wishes to thank Professor R. B. Bird of the University of Wisconsin, Madison, Wisconsin, for his introduction to the oscillating manometer problem. His suggestions and assistance were extremely helpful. Also, thanks should be given to Professor E. H. Wissler of the University of Texas, Austin, Texas, for loaning the author and Professor Bird a copy of the report describing an undergraduate research project on a non-Newtonian oscillating manometer. Financial support was received from National Science Foundation Grant G11996.

NOTATION

F_T = force at ends of liquid legs owing to flow reversal; dynes
F_{ST} = net force on moving fluid owing to surface tension; dynes
g_z = acceleration owing to gravity in axial direction; cm./sec.^{2}
h_a^*, h_b^* = height measurements
h_1 = left leg height above initial equilibrium position; cm.
h_2 = right leg height below initial equilibrium position; cm.
h = $(h_1 + h_2)/2$
h^* = dimensionless leg height; h/r_o
k = radial position for numerical integration
K_{ST} = surface tension, dynes/cm.
L = length of manometer fluid; cm.
L^* = dimensionless length of manometer fluid; L/r_o
m = time position for numerical integration
M = sign of average velocity in manometer
n = number of half cycles between height measurements, h_a^* and h_b^*
P = hydrostatic pressure; dynes/sq.cm.
$\mathcal{P}$ = combined static pressure and gravitational force; $P - \rho gz$
P^*_T = dimensionless pressure owing to flow reversal; $(4/3) \langle v^* \rangle \Omega_2$
P^*_{ST} = dimensionless pressure owing to surface tension; $(4/3) \langle v^* \rangle \Omega_3 M$
r = radial distance from center of tube; cm.
r_o = radius of tube; cm.
r^* = dimensionless radius, r/r_o
Δr^* = numerical integration radial increment
R = radius of manometer bend; cm.
s = sample standard deviation
S = cross-sectional area of tube; sq.cm.
t = time; sec.
t^* = dimensionless time; $t[(3/2)g/r_o]^{1/2}$
Δt^* = numerical integration time increment
v = fluid velocity; cm./sec.
v_r = fluid velocity in radial direction, cm./sec.
v_θ = fluid velocity in circumferential direction, cm./sec.
v_z = fluid velocity in axial direction, cm./sec.
v^* = dimensionless velocity; $v[(3/2)r_o g]^{-1/2}$
z = axial distance in tube; cm. .

Greek Letters

ζ = damping factor in second-order damped-harmonic differential equation
μ = Newtonian viscosity; dyne sec./sq.cm.
ϕ_R = contact angle of receding column
ϕ_A = contact angle of advancing column
ω_n = natural frequency of the system in second-order damped harmonic differential equation
Ω_1 = dimensionless reciprocal kinematic viscosity: $\left(\frac{\rho}{\mu}\right)\left(\frac{g r_o^3}{24}\right)^{1/2}$

Ω_2 = dimensionless flow reversal viscous drag force: $(3/8)^{1/2}K_T r_o \mu/(\rho g^{1/2})$

Ω_3 = dimensionless surface tension: $K_{ST}(\cos\phi_R - \cos\phi_A)/(r^2_o \rho g)$

$< >$ = quantity averaged over area of tube

ρ = fluid density, g./cc.

LITERATURE CITED

1. Bird, R. B., W. E. Stewart, and E. N. Lightfoot, "Transport Phenomena," 1 ed., pp. 229-231, Wiley, New York (1961).
2. Ceaglske, N. H., "Automatic Process Control for Chemical Engineers," 1 ed., pp. 75-76, Wiley, New York (1956).
3. Miller, G. E., "Transient State Flow of a Non-Newtonian Fluid," unpublished report, Univ. of Texas, Austin, Texas (1960).
4. Martin, R. J., and D. S. Moseley, *Trans. Am. Soc. Mech. Engrs.*, **80**, 1343-8 (1958).
5. Williams, T. J., *Trans. Am. Soc. Mech. Engrs.*, **78**, 1461-9 (1956).
6. McKennell, Raymond, "Proc. 2nd Intern. Congr. Rheol. 1953," p. 350, Butterworth's, London, England (1954).
7. Biery, J. C., and J. D. Huppler, "Newtonian and Non-Newtonian Viscosity Determinations on a Cone and Plate Viscometer," *Engineering Experiment Station Report No. 19*, Univ. of Wisconsin, Madison, Wisconsin (1962).
8. Hodgman, C. D., R. C. Weast, and M. S. Selby, editors, "Handbook of Chemistry and Physics," 42 ed., The Chemical Rubber Publishing Co., Cleveland, Ohio (1961).
9. Snedecor, G. W., "Statistical Methods," 5 ed., The Iowa State College Press, Ames, Iowa (1956).
10. Savant, C. J. Jr., "Basic Feedback Control System Design," 1 ed., p. 9, McGraw-Hill, New York (1958).
11. Hildebrand, F. B., "Introduction to Numerical Analysis," 1 ed., p. 75, McGraw-Hill, New York (1956).
12. Lamb, H., "Hydrodynamics," 6 ed., p. 622, Dover Publications, New York (1932).
13. Goldstein, S., ed., "Modern Developments in Fluid Dynamics," Vol. 1, pp. 312-314, Oxford Press, London, England (1950).

Manuscript received November 1, 1962; revision received March 1, 1963; paper accepted March 5, 1963.

The Dynamic Behavior of a Pulsed-Plate Extraction Column

JOHN W. WATJEN and ROBERT M. HUBBARD

University of Virginia, Charlottesville, Virginia

To achieve better design of automatically controlled systems, there is an increasing need to determine experimental data describing the dynamic behavior of chemical process equipment. Some few data have been published for countercurrent diffusional operations such as absorption (*1, 3, 4*) and extraction columns. Recently two papers (*2, 7*) have appeared describing the dynamic behavior of pulse-plate extraction columns based on both analog and digital computer solutions of mathematical models. The present work was undertaken to provide experimental dynamic extraction data to compare with linear theoretical models over the entire range of column flow conditions.

A pulsed-plate extraction column was chosen for the experimental work because variation of the column pulsation frequency allowed collection of data over a large range of mass transfer efficiency and fluid turbulence. The dynamic response of the system was measured with and without mass transfer to determine the effect of fluid flow on the overall column dynamics.

John W. Watjen is with E. I. DuPont de Nemours and Company, Incorporated, Wilmington, Delaware.

The theoretical linear-model response was determined by writing the general time-dependent differential material-balance equation for a model with mass transfer and fluid mixing and by solving the equivalent finite-difference equation using Laplace transforms. The solution gave the output as a function of signal frequency ($s = j\omega$) when the system was initially disturbed by a specific input such as a unit step or a pulse. At each value of signal frequency these results were expressed as the ratio of output-to-input amplitude (magnitude) and as the phase difference between the input and ouput.

At four column-pulsation frequencies, the experimental dynamic response was determined by the pulse method (*5*) for conditions of good mass transfer and of no mass transfer. The combined response was determined with a pulse of acid into the methyl isobutyl ketone, acetic acid, water system. The fluid-flow response was determined with a pulse of scarlet-red dye, which was insoluble in the methyl isobutyl ketone phase. The acid concentration was measured by titrating output samples, and the dye concentration was measured with a spectrophotometer. The flow rates, mass transfer stage efficiencies, and eddy